IEEE Photonics Journal
An IEEE Photonics Society Publication

Open Access

# Two-Beam Emitting Via a Single Subwavelength Metal Slit Surrounded by Mixed-Period Dielectric Grooves

Volume 5, Number 6, December 2013

Ying-jie Su
Hung-chun Chang, Senior Member, IEEE

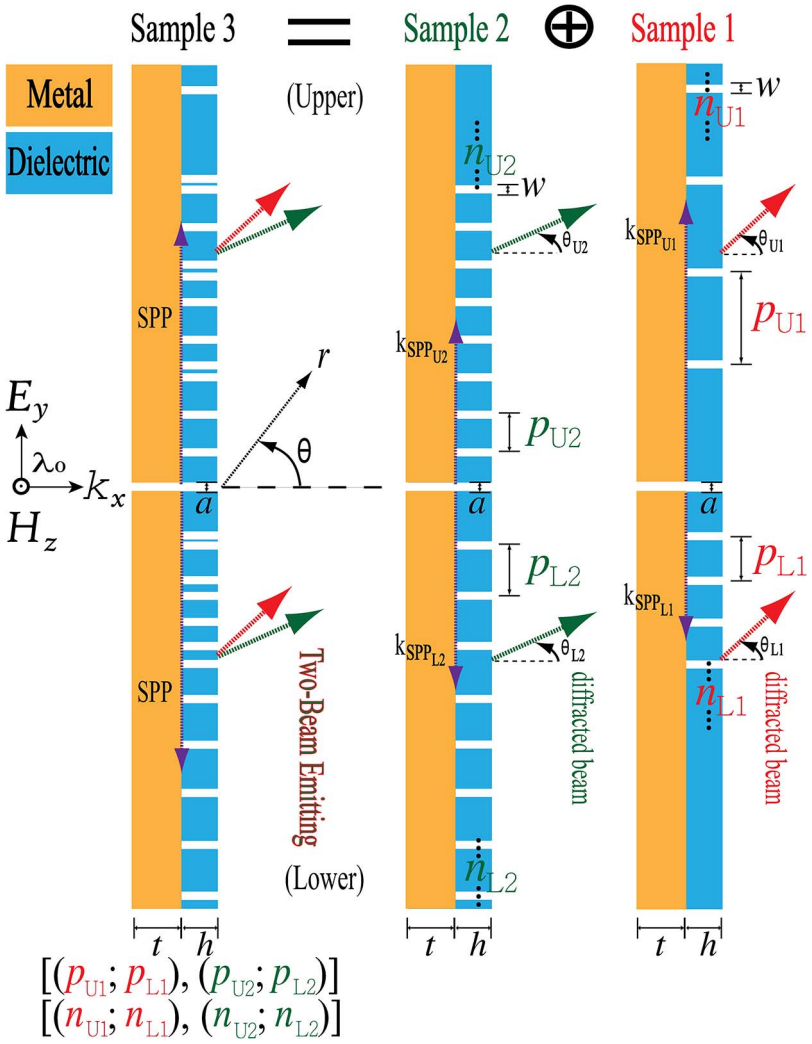


DOI: 10.1109/JPHOT.2013.2292352
1943-0655 

# Two-Beam Emitting Via a Single Subwavelength Metal Slit Surrounded by Mixed-Period Dielectric Grooves

**Ying-jie Su**[1] **and Hung-chun Chang,**[1,2,3] ***Senior Member, IEEE***

[1]Graduate Institute of Photonics and Optoelectronics, National Taiwan University, Taipei 10617, Taiwan
[2]Graduate Institute of Communication Engineering, National Taiwan University, Taipei 10617, Taiwan
[3]Department of Electrical Engineering, National Taiwan University, Taipei 10617, Taiwan

*DOI: 10.1109/JPHOT.2013.2292352*


Manuscript received September 13, 2013; revised November 5, 2013; accepted November 7, 2013. Date of current version December 2, 2013. This work was supported in part by the National Science Council of the Republic of China under Grants NSC 100-2221-E-002-182-MY2 and NSC 101-2221-E-002-147-MY2, by the Excellent Research Projects of National Taiwan University under Grant 102R89081, and by the Ministry of Education of the Republic of China under "The Aim of Top University Plan" Grant. Corresponding author: H.-C. Chang (e-mail: hcchang@cc.ee.ntu.edu.tw).

**Abstract:** We use mixed-period dielectric grooves to surround a single metal slit to realize two-beam nonsymmetrical and symmetrical emitting for the transmitted light emerged from the subwavelength slit. This proposed slit–groove-based structure is formed by combining two typical slit–groove structures, both possessing unidirectional beaming but with different beaming angles. Here, the typical slit–groove structure refers to the single slit perforated in the metal film, and the slit is surrounded by periodic dielectric grooves on the exit surface of the metal film. By using the finite-difference time-domain method, the simulation results show that two-beam emitting can be produced with flexible splitting angles via such combined structure. In addition, the power ratio of two-beam emitting can be changed via using appropriate groove number to surround the slit of the combined structure.

**Index Terms:** Beam splitters, diffraction and gratings, engineered photonics nanostructures, multibeam generation, subwavelength structures, surface plasmons.

## 1. Introduction

Owing to the wave nature of light, it is well known that light emerged from a subwavelength aperture (that is, aperture size smaller than the incident wavelength) usually diffracts in all directions. The above diffraction phenomenon thus limits the degree of photonic integrating, resulting in the size-compatibility problem between photonic and electronic devices at nanoscale dimensions [1], since the apertures such as holes or slits have been generally used as basic elements in photonic components. However, in 2002, it was experimentally reported that, when a subwavelength metal slit is surrounded by periodic surface grooves at the exit surface of the slit, the transmitted light emerged from the slit will concentrate as a beam with a small angular divergence. Such phenomenon for beaming light is called directional beaming [2]. Here, the typical slit-groove structure is with "symmetric" grooves, meaning that the periodic grooves on both sides of the slit have the same groove period. The feasibility of this concept has also been indicated to apply to microwaves [3], matter waves [4], and acoustic waves [5]. Such astounding finding for beaming light has attracted much attention [6]–[9] over the last decade because the directional beaming provides us a way to bypass the problem for the above-mentioned diffraction of light.

In recent years, the directional beaming for slit-groove structures made of dielectric and metal (that is, dielectric grooves surrounding a metal slit) has been studied [10], [11]. It has been found that such slit-groove structures can offer better performance for producing directional beaming than slit-groove structures made of purely metal [10]. In 2007, via the rigorous coupled-wave analysis (RCWA) method, it has been reported that off-axis beaming can be realized by using a typical slit-groove structure with "asymmetric" grooves which means the periodic grooves on both sides of the slit have different groove periods. Here, the structure was made of dielectric and metal as well [12]. Soon after, the off-axis beaming was further confirmed experimentally in the microwave regime [13]. Then, via the finite element method (FEM), it was investigated that the off-axis beaming can also be realized in the terahertz regime [14]. Afterwards, a designed method based on Huygens' principle was proposed for controlling the beaming angle of the off-axis beaming for application in edge-emitting laser diodes [15]. More recently, a plasmonic directional beaming device with an expected off-axis beaming angle has been presented experimentally [16].

In order to understand more about the underlying mechanisms for directional beaming, many works have investigated the interactions between the incident light and the typical slit-groove structure [17]–[19]. So far, some research groups have used Huygens' principle to theoretically study the directional beaming [6], [18], and others have proposed surface plasmon polariton (SPP) diffraction theory to physically explain the directional beaming [10], [20]. In fact, it has been generally believed that the surface waves play important roles for the directional beaming [8]. Inspired by the finding that using periodic grooves to surround the slit can produce directional beaming, that is, the surface waves can be steered via periodic surface corrugations, recently researchers have investigated various slit-groove-based structures with subwavelength features for producing beam-splitting or multiple-beam emitting for manipulating optical fields within nanoscale and/or microscale dimensions. These structures have been studied due to their potential applications in novel beam-splitters for highly dense photonic integrated circuits. Some results are available on producing two-beam symmetrical emitting [21]–[27]; however, the information about producing two-beam non-symmetrical emitting is limited [28]. Moreover, to our knowledge, no work has been made on combining two typical slit-groove structures to produce multiple beams.

In this study, we propose a slit-groove-based structure for realizing two-beam non-symmetrical and symmetrical emitting. The proposed structure consists of a single subwavelength slit perforated in a metal film, which is surrounded by mixed-period dielectric surface grooves that are made on the exit surface of the metal film. For convenience, we call the whole structure mixed-period slit-groove (MPSG) structure hereafter. In fact, the MPSG structure is formed by combining two similar typical slit groove structures with different groove periods. The details for the MPSG structure and simulation setup for our FDTD calculations will be given in Section 2. Section 2 also describes the SPP diffraction theory for deriving some basic formulae for verifying our numerical results. In Section 3, it is demonstrated that when the two typical directional-beaming slit-groove structures with different beaming angles are combined, two-beam non-symmetrical and symmetrical emitting can be created for the MPSG structure. In addition, it is shown that by changing the number of surrounding grooves for the two typical slit-groove structures to form the MPSG structure, the power ratio of the two-beam non-symmetrical emitting for the MPSG structure can be adjusted.

## 2. Modelling Structures, Theoretical Analysis, and Simulation Setup

### 2.1. Samples

The schematic of the MPSG structure, i.e., Sample 3, is shown in Fig. 1; this sample is formed by combining two typical slit-groove structures, i.e., Samples 1 and 2, as is also shown in Fig. 1. Each sample in Fig. 1 shows a penetrated subwavelength slit in a metal film, where the slit is surrounded by a finite number of dielectric surface grooves made on the exit surface of the metal film. Note that Samples 1 and 2 have similar geometries but different groove periods, namely $p_{U_1} \neq p_{U_2}$ and $p_{L_1} \neq p_{L_2}$. Under this condition, the combined structure (i.e., Sample 3) formed by combining Samples 1 and 2 shows mixed-period grooves surrounding the slit. In addition, Samples 1, 2, and 3

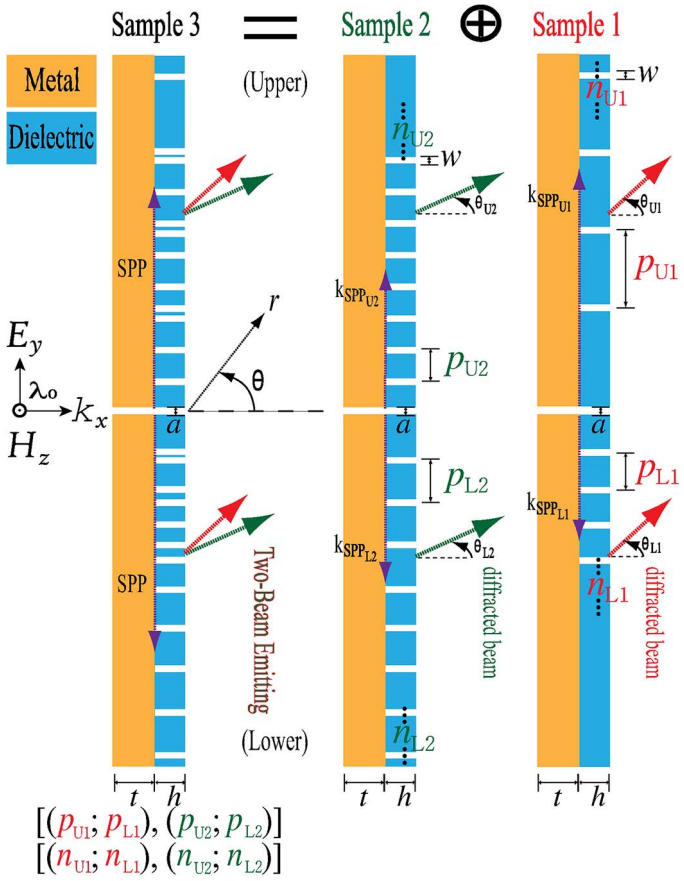


Fig. 1. Schematics of two typical slit-groove structures, i.e., Samples 1 and 2, and the combined structure (the MPSG structure), i.e., Sample 3. For Samples 1 and 2, the groove period and the groove number of the periodic grooves on the upper and the lower sides of the slit are denoted as $(p_{U_1}, n_{U_1})$, $(p_{L_1}, n_{L_1})$, $(p_{U_2}, n_{U_2})$, and $(p_{L_2}, n_{L_2})$. For Sample 3, the combined groove number and the combined groove pitches of the surrounding mixed-period grooves of the slit are denoted by the symbols of $[(p_{U_1}; p_{L_1}), (p_{U_2}; p_{L_2})]$ and $[(n_{U_1}; n_{L_1}), (n_{U_2}; n_{L_2})]$, respectively. For Samples 1 and 2 the slit width is $a$, metal-film thickness is $t$, the groove height (also the dielectric-layer thickness) is $h$, and the groove width is $w$. The impinging TM polarized light is at the wavelength of $\lambda_0$. The red and the green arrows denote the diffracted beams that arise from the diffraction of the SPPs.

in Fig. 1 have the same slit width, i.e., $a = 40$ nm, the same metal-film thickness, i.e., $t = 270$ nm, and the same groove height which is the dielectric-layer thickness, i.e., $h = 80$ nm.

The groove periods and the groove numbers of the periodic grooves on the upper side of the slit for Sample $i$ ($i = 1$ or 2) are denoted as $p_{U_i}$ and $n_{U_i}$, respectively, and those on the lower side are denoted as $p_{L_i}$ and $n_{L_i}$. The details of the groove periods for producing directional beaming for Samples 1 and 2 will be discussed in Section 3.1. Note that $n_{U_1} = n_{L_1} = 5$ and $n_{U_2} = n_{L_2} = 5$ are considered for Samples 1 and 2 for all situations discussed in Section 3 except the case in Fig. 6(d)–(f), as will be discussed in Section 3.2. Besides, all the grooves for Samples 1 and 2 have the same groove width, i.e., $w = 40$ nm. We emphasize again that Sample 3 is formed by combining Samples 1 and 2, and thus it is difficult to directly define the groove pitches and the groove numbers for the surrounding mixed-period grooves of Sample 3. Hence, we use the symbols, $[(p_{U_1}; p_{L_1}), (p_{U_2}; p_{L_2})]$ and $[(n_{U_1}; n_{L_1}), (n_{U_2}; n_{L_2})]$, to denote the combined groove pitches and the combined groove numbers for the mixed-period grooves for Sample 3, respectively.

### 2.2. Surface Plasmon Diffraction Theory

As was reported in previous publications, the typical slit-groove structures with symmetric grooves possess on-axis and multiple directional beaming [2], [8], [10], and the typical slit-groove

structures with asymmetric grooves possess off-axis beaming [12], [13]. From the physical point of view, the occurrence of these beaming effects can be attributed to the excitation of surface waves such as the SPPs by the slit and their coupling to diffracted beams through phase matching [6], [10], [20]. Such SPP diffraction theory is well known based on the following grating equations [10], [20]. For a typical slit-groove structure like Sample 1 or 2, the diffracted beams emitted from the upper and the lower sides of the slit are governed, respectively, by the following equations:

$$k_0 \sin\theta_U \hat{\mathbf{y}} = k_{SPP_U} \hat{\mathbf{y}} - m_U \frac{2\pi}{p_U} \hat{\mathbf{y}} \tag{1a}$$

$$k_0 \sin\theta_L \hat{\mathbf{y}} = k_{SPP_L} (-\hat{\mathbf{y}}) - m_L \frac{2\pi}{p_L} (-\hat{\mathbf{y}}). \tag{1b}$$

In (1), $\theta_U$, $m_U (= 0, \pm 1, \pm 2, \pm 3, \ldots)$, and $p_U$ are the diffraction angle, the diffraction order, and the groove period for the diffracted beam from the upper side of the slit, respectively, $\theta_L$, $m_L (= 0, \pm 1, \pm 2, \pm 3, \ldots)$, and $p_L$ are the corresponding quantities from the lower side of the slit, $k_0$ is wavenumber of the diffracted beams in free space, $\hat{\mathbf{y}}$ refers to the coordinates shown in Fig. 1, and $k_{SPP_U}$ and $k_{SPP_L}$ are real parts of the complex wavenumbers of the SPPs. Equation (1) describes how the SPPs are decoupled into light in the free space via the surrounding periodic grooves which act like gratings. Note that the SPP dispersion relation are altered by the groove height or surface corrugation/roughness caused by the undulated surfaces on both sides of the slit [20]. Such change of the SPP dispersion relation results from the multiple scattering [29]. For Samples 1 and 2, one thus assumes $k_{SPP_U} = k_{SPP_L} = k_{SPP}$ because the heights of grooves on both sides of the slit are the same. Also note that when the SPPs on both sides of the slit radiate light or diffracted beams in the same direction, namely $\theta_U = \theta_L = \theta$ $(-90^\circ < \theta < 90^\circ)$, the strong beaming phenomena can be observed for Sample 1 or 2.

In order to use the diffraction theory to verify our FDTD simulation results for Sample 1 or 2 in the later sections, some theoretical results by considering $p_U = p_L$ and $p_U \neq p_L$ are derived via (1), as discussed in the following. First, consider $p_U = p_L = p$ for Sample 1 or 2. In this case, strong two-beam symmetrical emitting can be observed when $\theta_U = \theta_L = \theta$. By considering $k_{SPP_U} = k_{SPP_L} = k_{SPP}$ as mentioned above, it can be derived from (1) that the groove period $p$ for producing strong beaming for Sample 1 or 2 satisfies the following relation:

$$p = \pi (m_U + m_L) k_{SPP}^{-1}. \tag{2}$$

In fact, for a typical slit-groove structure with symmetric grooves, it has been pointed out that the on-axis beaming and the multiple directional beaming such as two-beam symmetrical emitting, can be attributed to the superimposing of the first-order diffracted beams (i.e., $m_U = 1$ and $m_L = 1$) and the superimposing of the first-order and the second-order diffracted beams (i.e., $m_U = 1$ and $m_L = 2$, and $m_U = 2$ and $m_L = 1$) emerged from both sides of the slit, respectively [8]. With these points in mind, from (2) one can know that the on-axis beaming and the two-beam symmetrical emitting occur for the typical slit-groove structure, respectively, when this structure is with the groove period of $p^{(\text{on-axis})} = 2\pi k_{SPP}^{-1}$ and $p^{(\text{two-beam})} = 3\pi k_{SPP}^{-1}$. Accordingly, based on the diffraction theory, one concludes that the ratio of $p^{(\text{two-beam})}$ to $p^{(\text{on-axis})}$ is 1.5. This ratio will be used to check our simulation results as will be shown in Section 3.1.

Second, consider $p_U \neq p_L$ for Sample 1 or 2. In this case, a unidirectional off-axis beaming can be observed when both sides of the slit emit the diffracted beams in the same deviation angle with respective to the on-axis. Similarly, by considering $\theta_U = \theta_L = \theta$ and $k_{SPP_U} = k_{SPP_L} = k_{SPP}$, the off-axis beaming angle derived from (1) is

$$\theta = \left\{ \sin^{-1} \left[ \lambda_0 \left( \frac{m_L p_U - m_U p_L}{2 p_U p_L} \right) \right] \right\} \left( \frac{180^\circ}{\pi} \right). \tag{3}$$

The result of (3) will also be used to check our FDTD simulation results in Section 3.1.

So far, the beaming behaviors for Sample 1 or 2 have been analyzed by using the diffraction theory. Actually, the grating equation cannot be directly applied to analyze the diffraction behavior of the SPPs for Sample 3. Intuitively, it is a natural thought to consider Sample 3 may possess no beaming effects, owing to that the mixed-period grooves appear to possess no periodicities. However, our FDTD simulation results in Section 3.2 will demonstrate that Sample 3 possesses significant beaming phenomena.

### 2.3. Setup in the FDTD Program

A two-dimensional FDTD method [30] was used to calculate the electromagnetic (EM) fields for Samples 1, 2, and 3 in Fig. 1. This numerical approach is a powerful tool for solving EM problems containing media with irregular geometries such as the surrounding mixed-period grooves of Sample 3. In our FDTD simulations, the discretization grid spacing was set to be 2.5 nm in both the $x$ and $y$ directions. The computational domain was set to be with 16-$\mu$m width in the $x$ direction and 24-$\mu$m width in the $y$ direction. A plane wave was considered (set at $x = 0.02$ $\mu$m) to normally impinge on the input surface of Samples 1, 2, and 3. The incident wavelength was taken to be $\lambda_0 = 532$ nm and the light source was set to be of the TM polarization with the magnetic field parallel to the $z$ direction in order to excite the SPPs.

In order to absorb the outgoing EM waves scattered from Samples 1, 2, and 3, the perfectly matched layers (PMLs) [30] were put on the boundaries to surround the computational domain along the $x$ and $y$ directions. The edges of Samples 1, 2, and 3 are extended through the perfectly matched layers along the $y$ direction, that is, these samples are assumed to have infinite lengths in the $y$ direction. Under this condition, the effects of the disturbance from the edge, such as light emerged from the upper and the lower edges of the sample to interfere with the light emerged from the slit, can be ignored. The exit surface, which is the interface between the metal and the dielectric, and the slit centerline of Samples 1, 2, and 3 were set at $x = 1.17$ $\mu$m and $y = 12.05$ $\mu$m, respectively. For all samples in Fig. 1, the metal portions are made of silver with the refractive index of $0.13 + j3.19$ at $\lambda_0 = 532$ nm [31], and the dielectric portions are with the refractive index of 1.72 [12]. In our FDTD simulations, we use the Drude model to approximate the dispersive permittivity of the metallic film, namely,

$$\epsilon(\omega) = \epsilon_\infty - \frac{\omega_p^2}{\omega^2 + j\gamma\omega}. \tag{4}$$

In (4), $\omega$ is the angular frequency of the impinging light, $\epsilon_\infty$ is the relative permittivity at infinite frequency, $\omega_p$ is the plasma frequency, and $\gamma$ is the damping constant. In our FDTD program, these Drude parameters are taken to be $\epsilon_\infty = 5$, $\omega_p = 1.38158 \times 10^{16}$ s$^{-1}$, and $\gamma = 1.93855 \times 10^{14}$ s$^{-1}$ for silver at $\lambda_0 = 532$ nm.

From the FDTD calculated EM fields, which are in the form of phasor fields, the angular transmittances for Samples 1, 2, and 3 can be determined. Here, the angular transmittance refers to the angular distribution of the energy flux or Poynting vector of the transmitted light emitted from the subwavelength slit. By the definition in the EM theory, the time-averaged Poynting vector can be expressed as

$$\tilde{\mathbf{S}}(r,\theta) = \frac{1}{2}\Re\left[\tilde{\mathbf{E}}(r,\theta) \times \tilde{\mathbf{H}}^*(r,\theta)\right]. \tag{5}$$

In (5), $r$ is the radial coordinate, $\theta$ is the polar angle, $\tilde{\mathbf{E}}$ is the electric field phasor, and $\tilde{\mathbf{H}}^*$ is the complex conjugate of the magnetic field phasor. Based on the calculated time-averaged Poynting vector, the angular transmittances can be determined for Samples 1, 2, and 3. The angular transmittance $I$ is defined as

$$I(\theta) = \left.\frac{\left|\tilde{\mathbf{S}}(r,\theta)_N \cdot \hat{\mathbf{r}}\right|}{\left|\tilde{\mathbf{S}}(r,\theta)_{N=0} \cdot \hat{\mathbf{r}}\right|}\right|_{r=10^{-5}\,m}. \tag{6}$$

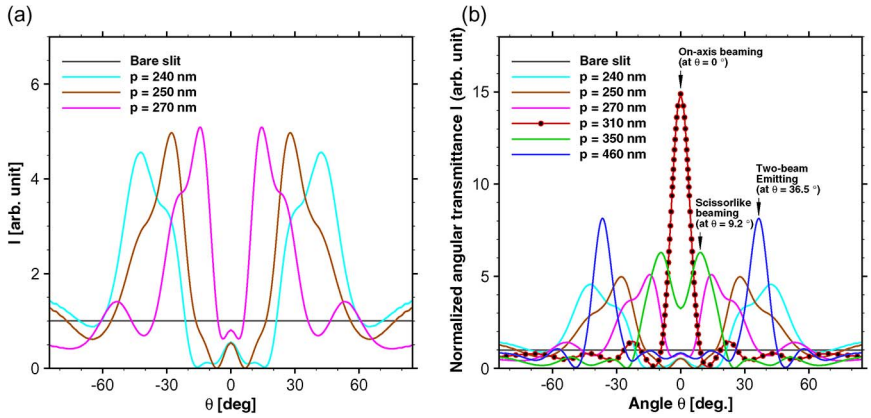


Fig. 2. Angular transmittance distributions $I$ for Sample 1 or 2 with symmetric groove $(p_U = p_L = p)$ for (a) $p = 0$ (the bare slit), 240, 250, and 270, and (b) $p = 310$, 350, and 460 nm, where $a = w = 40$ nm, $t = 270$ nm, $h = 80$ nm, and $n_{U_1} = n_{L_1} = n_{U_2} = n_{L_2} = 5$. The red curve with dots is associated with on-axis beaming.

Here, $\hat{\mathbf{r}}$ is the radial unit vector in the cylindrical coordinates, $\tilde{\mathbf{S}}(r,\theta)_N$ is the Poynting vector for the transmitted light for the sample with $N$ grooves, and $\tilde{\mathbf{S}}(r,\theta)_{N=0}$ is that for the one with all the grooves removed such that all the surface indentations are filled with dielectric for this sample, or the case with the bare slit. The detectors were positioned at $r = 10^{-5}$ meters in order to record the Poynting vector of the transmitted light.

## 3. Numerical Results and Discussion

In order to set appropriate groove periods for Samples 1 and 2 to produce directional beaming, Section 3.1 begins with examining the angular transmittance distributions for a typical slit-groove structure by varying groove periods. After that, we will combine Samples 1 and 2 with appropriate groove periods for producing strong beaming with different beaming angles to form Sample 3, and explore the diffraction behaviors of the transmitted light emitted from the subwavelength slit of Sample 3, as will be investigated in Section 3.2. In particular, three types of two-beam non-symmetrical emitting will be realized based on Sample 3 with the mixed-period grooves.

### *3.1. Directional On-Axis and Off-Axis Beaming From Samples 1 and 2*

We first analyze the angular transmittance distribution for a typical slit-groove structure like Sample 1 or 2 by considering $p_U = p_L = p$. The angular transmittances for the typical slit-groove structure for different $p$'s are shown in Fig. 2. The gray curve in Fig. 2(a) or (b), which shows the transmittance $I = 1$ over the whole spectrum, is the calculated angular transmittance distribution for the bare-slit case. This curve is plotted as a reference transmittance, and the corresponding magnetic field intensity distribution is shown in Fig. 3(a) as the reference field. Fig. 3(a) shows that the transmitted light emerged from the slit is with a broad angular distribution. In other words, the transmitted light behind the bare slit diffracts almost uniformly in all directions. Such diffraction phenomenon is a characteristic of a subwavelength slit. Note that the ratio of $\lambda_0$ to $a$ is 13.3 in this case. However, it is seen in the inset of Fig. 3(a) that some (energy) of the transmitted light is confined by the SPPs at the metal-dielectric interfaces instead of being diffracted. The SPPs are launched because of the subwavelength feature of the slit [32], [33]. The SPPs are evanescent in the near field. Due to lack of surface corrugations such as periodic grooves on both sides of the slit, no beaming effects are observed in Fig. 3(a) for the bare slit.

Next, we examine the diffraction behaviors behind the slit for the typical slit-groove structures with increasing groove period, such as $p = 240$, 250, and 270 nm, and the corresponding angular transmittance distributions are shown as the cyan, the brown, and the pink curves in Fig. 2(a),

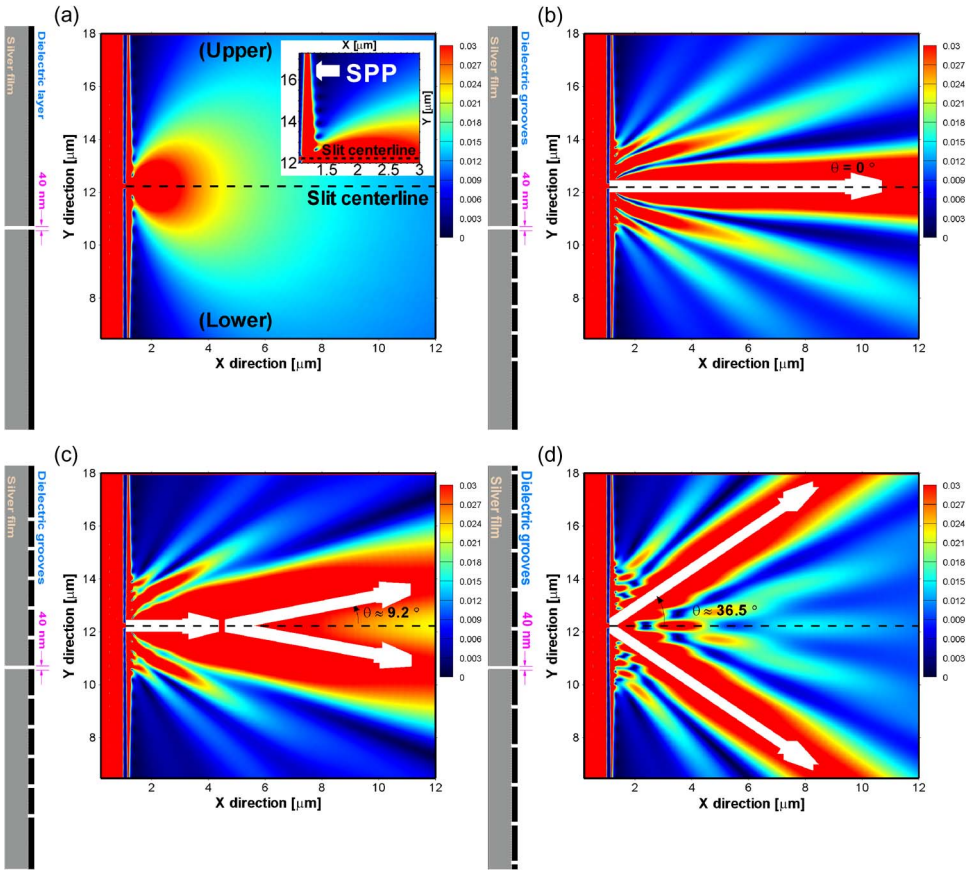


Fig. 3. Magnetic field intensity $|H_z|$ distributions for the same sample in Fig. 2 for $p =$ (a)0, (b) 310, (c) 350, and (d) 460 nm. The inset near the left of each panel shows the corresponding structure. The inset in the right-upper corner of (a) shows the nonradiative SPP confined at the metal-dielectric interface.

respectively. In Fig. 2(a), the cyan, the brown, and the pink curves respectively show dual peaks at $\theta \approx \pm 42.2^\circ$, $\pm 27.7^\circ$, and $\pm 14.4^\circ$. The peaks at the angles for $\theta < 0^\circ$ and $\theta > 0^\circ$ for the three curves are due to the diffractions of the SPPs located on the upper and the lower sides of the slit, respectively. It is obvious that the shapes for the above-mentioned dual peaks are not of single-peak characteristic since the diffracted beams from both sides of the slit are not both emitted at the diffraction angles associated with the dual peaks. In other words, the beaming effects for the typical slit-groove structure for $p = 240$, 250, and 270 nm are relatively weak.

From the dual peaks of the curves for $p = 240$, 250, and 270 nm in Fig. 2(a), one can see that the larger the groove period, the closer the two peaks. Accordingly, one may deduce that a single peak may appear for the angular transmittance distribution for the typical slit-groove structure when the groove period is sufficiently large. Therefore, we increased the groove period from $p = 270$ to 310 nm and the angular transmittance distribution for $p = 310$ nm is shown as the red curve with dots in Fig. 2(b), which shows a single narrow peak with high transmittance appears at $\theta = 0^\circ$. The corresponding magnetic field intensity distribution is shown in Fig. 3(b), which clearly presents the transmitted light emitted from the slit forms a strong on-axis beaming propagating in the direction normal to the exit surface of the film. The occurrence of this strong beaming is due to that the diffracted beams or waves from both sides of the slit are emitted in the same direction, and interfere constructively.

When we continue to increase the groove period to $p = 350$ and 460 nm, the angular transmittance distributions for the typical slit-groove structure show dual peaks again, as plotted as the green and the blue curves in Fig. 2(b), respectively, and the magnetic field intensity distributions

are shown in Fig. 3(c) and (d), respectively. From Fig. 3(c) [scissor-like beaming] and (d) [two-beam emitting] it is clear that the dual peaks for the green and the blue curves in Fig. 2(b) are owing to the diffracted beams from both sides of the slit. In addition, we notice that the two-beam symmetrical emitting in Fig. 3(d) is similar to the result for the two directional beaming as reported in [8], although the typical slit-groove structure investigated in this work is made of real metal and dielectric instead of the purely perfect electric conductor as investigated in [8]. In fact, by calculating the ratio of the groove period associated with the two-beam emitting of Fig. 3(d) for $p = 460$ nm to the groove period associated with the on-axis beaming of Fig. 3(b) for $p = 310$ nm, the ratio 1.48 is in a good agreement with the theoretical result of 1.5 as was predicted in Section 2.2 via (2). Accordingly, the two-beam emitting in Fig. 3(d) confirms that the multiple directional beaming phenomenon not only occurs for a metal slit surrounded with symmetric metal grooves but also a metal slit surrounded with symmetric dielectric grooves.

In short, from Fig. 3(b)–(d) it is confirmed that the diffraction angles of the diffracted beams from both sides of the slit can be changed by fine-tuning the groove periods of the surrounding grooves of the typical slit-groove structure. On the other hand, it is possible to produce a significant off-axis beaming by choosing appropriate $p_U$ and $p_L$ for the slit-groove structure, as long as these groove periods make the diffracted beams from both sides of the slit emit in the same off-axis angle. For the purpose of creating the unidirectional off-axis beaming, next we examine the diffraction behavior for the typical slit-groove structure by considering $p_U \neq p_L$.

For example, first recall that the angular transmittance distribution for the typical slit-groove structure with $p_U = p_L = 350$ nm shows the dual peaks at $\theta \approx \pm 9.2^\circ$, referring to the green curve in Fig. 2(b). Then, we gradually decrease $p_L$ from 350 nm to adjust the diffraction angle of the diffracted beam from the lower side of the slit. The angular transmittance distributions for the typical slit-groove structure with several smaller $p_L$'s are shown in Fig. 4(a1). A single narrow peak at $\theta \approx 10.7^\circ$ with high transmittance is observed in the red curve with dots of Fig. 4(a1) with $p_U = 350$ nm and $p_L = 290$ nm. The corresponding magnetic field intensity distribution is shown in Fig. 4(a2), which shows clearly an off-axis beaming at $\theta \approx 10.7^\circ$. This directional beaming is owing to that the diffracted beams emitted from both sides of the slit interfere constructively in almost the same direction at $\theta \approx 10.7^\circ$.

Also recall that the blue curve in Fig. 2(b) with $p_U = p_L = 460$ nm shows the dual peaks at angles $\theta \approx \pm 36.5^\circ$. We also gradually decrease $p_L$ from 460 nm and the angular transmittance distributions for the typical slit-groove structure with several smaller $p_L$'s are shown in Fig. 4(b1). Similarly, a single narrow peak at $\theta \approx 37.2^\circ$ with high transmittance is observed in the red curve with dots of Fig. 4(b1) with $p_U = 460$ nm and $p_L = 240$ nm. As expected, the corresponding magnetic field intensity distribution shown in Fig. 4(b2) appears to have an off-axis beaming as well at $\theta \approx 37.2^\circ$.

So far, we have found out four parameter sets for the groove periods $p_U$ and $p_L$ for designing Sample 1 or 2 to give directional beaming at four different beaming angles. The four parameter sets and the corresponding beaming angles are summarized in Table 1. The beaming angles predicted by (3) are also shown in Table 1 for checking the FDTD calculated beaming angles. Inspection of beaming angles presented in Table 1 shows that the agreement between our FDTD numerical results and the theoretical predictions is fairly good. The difference in the beaming angle between the theoretical and the numerical results could be attributed to the finite-size effect of the gratings with finite groove numbers on both sides of the slit, since (3) is derived for a grating with infinite number of grooves rather than a finite number of grooves.

We have also conducted the following examination. We vary the dielectric thickness for the above-mentioned Sample 1 or 2 to observe the influence of $k_{SPP}$ on the beaming phenomenon. As an example, we calculate the transmittance angular distributions for Sample 1 or 2 with $p_U = 350$ nm and $p_L = 290$ nm (namely, Set A in Table 1) for $h = 80$, 100, 120, and 140 nm. The FDTD calculated results are shown in Fig. 5. From Fig. 5 it is clear that Sample 1 or 2 with different dielectric-layer thicknesses shows different beaming phenomena. For example, the blue curve for $h = 120$ nm shows a splitting peak, unlike the red curve for $h = 80$ nm shows a single peak. Such result could be understood via (2) and (3). It can be seen in (2) that the groove period for producing a strong beaming is a function of $k_{SPP}$, and in (3) that the off-axis beaming angle is dependent on the groove period.

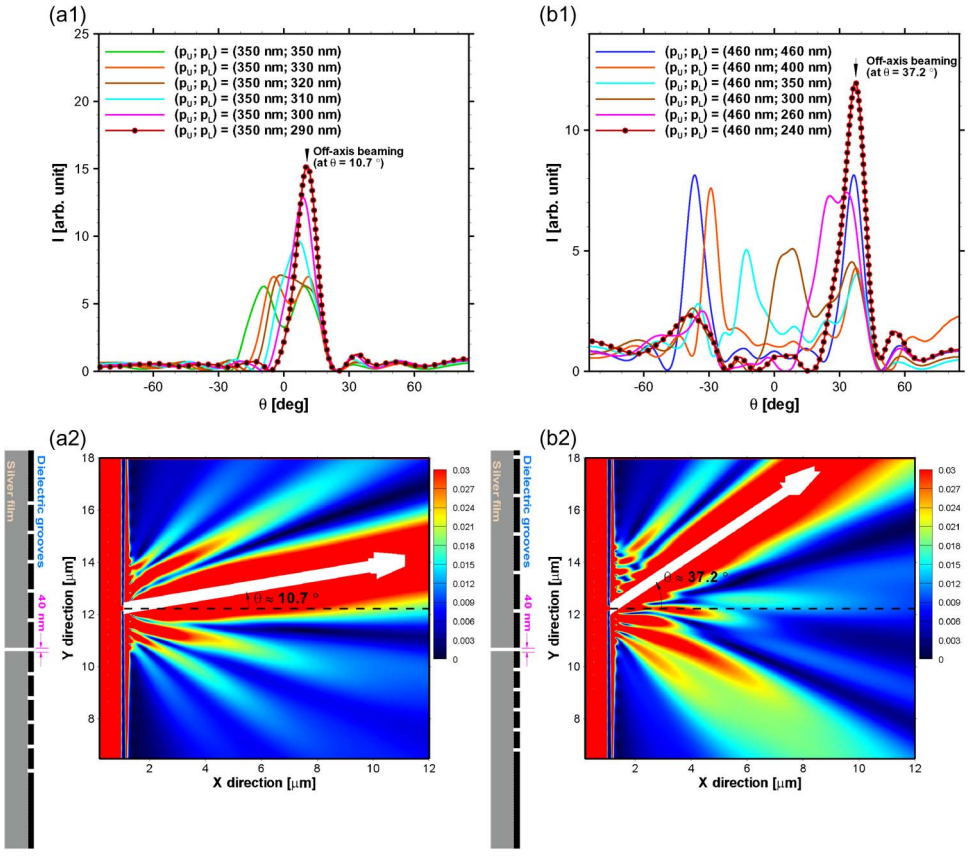


Fig. 4. Angular transmittance distributions $I$ for Sample 1 or 2 with asymmetric groove sets. All geometrical parameters are the same as in Fig. 2 except (a1) $p_U = 350$ nm and $p_L = 350$, 330, 320, 310, 300, and 290 nm, and (b1) $p_U = 460$ nm and $p_L = 460$, 400, 350, 300, 260, and 240 nm. The red curve with dots is associated with off-axis beaming. (a2) Magnetic field intensity $|H_z|$ distribution for $p_U = 350$ nm and $p_L = 290$ nm. (b2) $|H_z|$ distribution for $p_U = 460$ nm and $p_L = 240$ nm. The inset near the left of each panel shows the corresponding structure.

TABLE 1

Four parameter sets for $p_U$ and $p_L$ for Sample 1 or 2 at $\lambda_0 = 532$ nm. The third and the fourth rows show the beaming angles calculated by the FDTD method and predicted by the SPP grating diffraction theory, respectively. In (3), the diffraction orders are considered to be $m_U = 1$ and $m_L = 1$

| Parameter sets | Set A | Set B | Set C | Set D |
|---|---|---|---|---|
| Periods, $(p_U; p_L)$ [nm] | $(350; 290)$ | $(290; 350)$ | $(310; 310)$ | $(460; 240)$ |
| Beaming angles (FDTD) | $\theta_A \approx 10.7°$ | $\theta_B \approx -10.7°$ | $\theta_C = 0°$ | $\theta_D \approx 37.2°$ |
| Beaming angles [(3)] | $\theta \approx 9.0°$ | $\theta \approx -9.0°$ | $\theta = 0°$ | $\theta \approx 32°$ |

Accordingly, based on (2) and (3), it can be concluded that the beaming phenomenon should be dependent on $k_{SPP}$.

### 3.2. Two-Beam Non-Symmetrical and Symmetrical Emitting for Sample 3

After verifying the numerical results, next we explore the beaming effects for Sample 3. This subsection shows that via selecting appropriate groove periods for Samples 1 and 2 for producing directional beaming, two-beam non-symmetrical and symmetrical emitting can be achieved by the corresponding combined sample, i.e., Sample 3. The following will present three conditions for the two-beam non-symmetrical emitting for Sample 3. The following Samples 3 are formed by combining Samples 1 and 2 by considering $p_{U1} \neq p_{L2}$ and $p_{U2} \neq p_{L1}$.

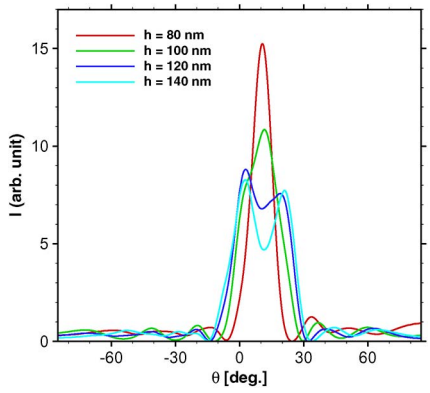


Fig. 5. Angular transmittance distributions $I$ for Sample 1 or 2 with different dielectric-layer thicknesses for $h = 80$, 100, 120, and 140 nm. All geometrical parameters are the same as Sample 1 or 2 in Fig. 4(a1) for the red curve with dots except $h$.

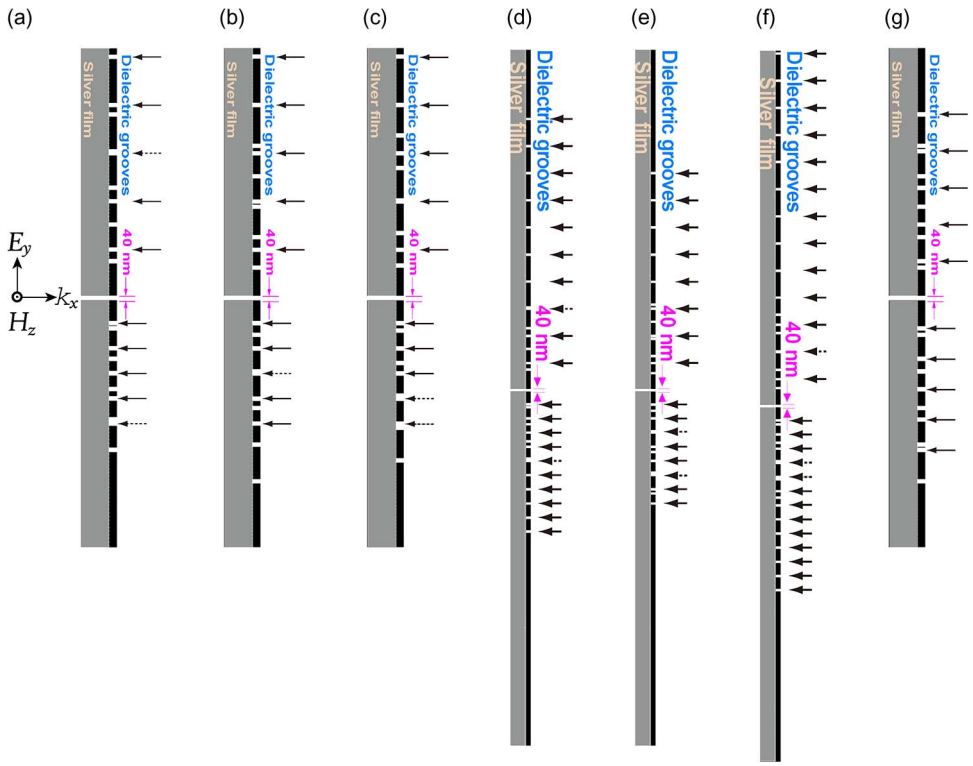


Fig. 6. Structures of Samples 3 with the mixed-period grooves for different groove pitches and groove numbers. The first three Samples 3 are formed by combining Samples 1 with (a) $p_{U_1} = 350$ nm and $p_{L_1} = 290$ nm, (b) $p_{U_1} = 290$ nm and $p_{L_1} = 350$ nm, and (c) $p_{U_1} = 310$ nm and $p_{L_1} = 310$ nm, respectively, and Sample 2 with $p_{U_2} = 460$ nm and $p_{L_2} = 240$ nm, where $n_{U_1} = n_{L_1} = n_{U_2} = n_{L_2} = 5$. The fourth, the fifth, and the sixth Samples 3 are formed by combining the same Samples 1 and 2 used in (a), (b), and (c) but with different groove numbers, namely (d) $n_{U_1} = n_{L_1} = 4$ and $n_{U_2} = n_{L_2} = 10$, (e) $n_{U_1} = n_{L_1} = 5$ and $n_{U_2} = n_{L_2} = 8$, and (f) $n_{U_1} = n_{L_1} = 5$ and $n_{U_2} = n_{L_2} = 13$, respectively. (g) The last Sample 3 is formed by combining Sample 1 with $p_{U_1} = 290$ nm and $p_{L_1} = 350$ nm and Sample 2 with $p_{U_2} = 350$ nm and $p_{L_2} = 290$ nm, where $n_{U_1} = n_{L_1} = n_{U_2} = n_{L_2} = 5$. The other geometrical parameters of all the above-mentioned samples are the same, i.e., $a = w = 40$ nm, $t = 270$ nm, and $h = 80$ nm. For the mixed-period grooves of each Sample 3, the grooves associated only with Sample 2 are indicated by arrows with solid lines, the grooves associated with both Samples 1 and 2 (that is, overlapping grooves) are indicated by arrows with dashed lines, and other grooves are associated with Sample 1 only.

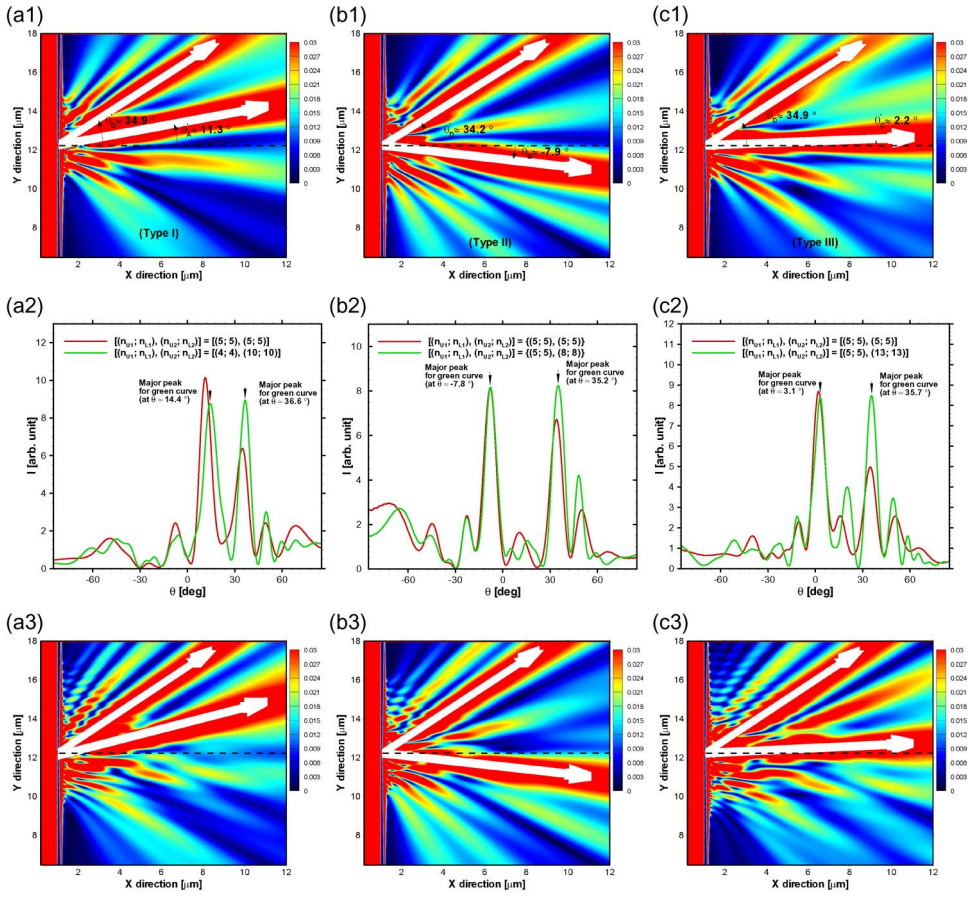


Fig. 7. (a1), (b1), (c1), (a3), (b3), and (c3) show magnetic field intensity $|H_z|$ distributions for the same Sample 3 in Fig. 6(a)–(f), respectively. In (a2), (b2), and (c2), the red and the green curves, respectively, show angular transmittance distributions *I* for the same Sample 3 in Fig. 6(a)–(f).

First, we select the parameters for Sets A and D from Table 1 as the groove periods for Samples 1 and 2, respectively, to form Sample 3, as is shown in Fig. 6(a). The magnetic field intensity distribution for Sample 3 is shown in Fig. 7(a1), demonstrating that the transmitted light emerged from the slit forms two beams. Note that both beams appear on the upper side of the slit centerline. In order to know the splitting angles for the two-beam emitting, the angular transmittance distribution for Sample 3 is presented as the red curve in Fig. 7(a2). From the two major peaks of the red curve it is clear that the splitting angles for the lower and the upper beams for the non-symmetrical emitting in Fig. 7(a1) are $\theta'_A \approx 11.3^\circ$ and $\theta'_D \approx 34.9^\circ$, respectively.

Second, we select the parameters for Sets B and D from Table 1 as the groove periods for Samples 1 and 2, respectively, to form Sample 3, as is shown in Fig. 6(b). The magnetic field intensity distribution for Sample 3 is shown in Fig. 7(b1). The transmitted light emerged from the slit also forms two beams, however in this case one beam appears on the lower side of the slit centerline and the other appears on the upper side. The angular transmittance distribution for Sample 3 is presented as the red curve in Fig. 7(b2). The two major peaks of the red curve show that the splitting angles for the lower and the upper beams for the non-symmetrical emitting in Fig. 7(b1) are $\theta'_B \approx -7.9^\circ$ and $\theta'_D \approx 34.2^\circ$, respectively.

Third, we select the parameters for Sets C and D from Table 1 as the groove periods for Samples 1 and 2, respectively, to form Sample 3, as is shown in Fig. 6(c). The magnetic field intensity distribution for Sample 3 is shown in Fig. 7(c1). The transmitted light emerged from the slit forms two beams as well, but now the lower beam of the two is produced to emit almost with the angle of $\theta = 0^\circ$.

TABLE 2

Three types of two-beam non-symmetrical emitting for Type I in Fig. 7(a1), Type II in Fig. 7(b1), and Type III in Fig. 7(c1) for Samples 3 at $\lambda_0 = 532$ nm. Sample 3 is formed by combining Sample 1 with $(p_{U1}; p_{L1})$ and Sample 2 with $(p_{U2}; p_{L2})$. The second row shows a combination of the parameter sets for the groove periods, selected from Table 1. The third row shows the splitting angles calculated by the FDTD method

| Beaming types | Type I | Type II | Type III |
|---|---|---|---|
| $[(p_{U_1}; p_{L_1}), (p_{U_2}; p_{L_2})]$ (nm) | $[(350; 290), (460; 240)]$ | $[(290; 350), (460; 240)]$ | $[(310; 310), (460; 240)]$ |
| Beaming angles | $[\theta'_A \approx 11.3^\circ, \theta'_D \approx 34.9^\circ]$ | $[\theta'_B \approx -7.9^\circ, \theta'_D \approx 34.2^\circ]$ | $[\theta'_C \approx 2.2^\circ, \theta'_D \approx 34.9^\circ]$ |

As indicated by the left major peak of the red curve in the corresponding angular transmittance distribution in Fig. 7(c2), the splitting angle for the lower beam is $\theta'_C \approx 2.2^\circ$. The right major peak of this red curve shows that the splitting angle for the upper beam is $\theta'_D \approx 34.9^\circ$.

According to the locations of the two beams relative to the slit centerline, the two-beam non-symmetrical emitting produced by Sample 3 could be classified into three types, called Types I, II, and III hereafter, referring to the two beams emitting on the same side of the slit centerline, on different sides of the slit centerline, and with one beam nearly along the slit centerline (an on-axis-like beaming), as demonstrated in Fig. 7(a1), (b1), and (c1), respectively. For convenience, the groove periods and the splitting angles for Types I, II, and III for these Samples 3 are summarized in Table 2.

Now we examine the similarities between the two-beam emitting produced by Sample 3 and the unidirectional beaming produced by the corresponding Samples 1 and 2. We compare the splitting angles in Table 2 with the corresponding beaming angles calculated by the FDTD method in Table 1, i.e., $\theta'_A \approx 11.3^\circ$ with $\theta_A \approx 10.7^\circ$ and $\theta'_D \approx 34.9^\circ$ with $\theta_D \approx 37.2^\circ$ for Type I, $\theta'_B \approx -7.9^\circ$ with $\theta_B \approx -10.7^\circ$ and $\theta'_D \approx 34.2^\circ$ with $\theta_D \approx 37.2^\circ$ for Type II, and $\theta'_C \approx 2.2^\circ$ with $\theta_C \approx 0^\circ$ and $\theta'_D \approx 34.9^\circ$ with $\theta_D \approx 37.2^\circ$ for Type III, respectively, and we find that the splitting angles of the lower and the upper beams for Sample 3 are respectively similar to the beaming angles of the corresponding Samples 1 and 2. Accordingly, we conclude that Sample 3 could be created to possess two-beam emitting with flexible splitting angles via combining Samples 1 and 2, as long as Samples 1 and 2 are designed to possess unidirectional beaming with desired beaming angles. Also, the above-mentioned results for the similarities of beaming angles imply that the two-beam non-symmetrical emitting is resulting from the constructive interference of diffracted beams emitted from both sides of the slit of Sample 3. Specifically, the upper grooves of Sample 3 emit two diffracted beams with different directions to constructively interfere with the ones emitted from the lower side of Sample 3, thus leading to the two-beam non-symmetrical emitting.

We also investigate the power ratios for the two-beam non-symmetrical emitting for Types I, II, and III. For the two major peaks of the red curve in Fig. 7(a2), (b2), or (c2), the power ratio is defined as the ratio of the peak value of the major peak which has the larger angular transmittance to the peak value of the other major peak. Thus, from the red curves in Fig. 7(a2), (b2), and (c2), it is clear that the power ratios for Types I, II, and III are about 1.6 (the ratio of $T \approx 10.1$ for the major peak at $\theta'_A \approx 11.3^\circ$ to $T \approx 6.4$ for the one at $\theta'_D \approx 34.9^\circ$), 1.2 (the ratio of $T \approx 8.1$ at $\theta'_B \approx -7.9^\circ$ to $T \approx 6.7$ at $\theta'_D \approx 34.2^\circ$), and 1.74 (the ratio of $T \approx 8.7$ at $\theta'_C \approx 2.2^\circ$ to $T \approx 5$ at $\theta'_D \approx 34.9^\circ$), respectively. Apparently, the power ratios for Types I, II, and III are all not equal to unity. This can be understood by the diffraction efficiency as in the following. Samples 1 and 2 have different groove periods, that is, $p_{U_1} \neq p_{U_2}$ and $p_{L_1} \neq p_{L_2}$, and therefore the surrounding gratings of Sample 1 and those of Sample 2 have different diffraction efficiencies. In this case, the unidirectional beaming produced by Sample 1 and the one produced by Sample 2 have different beaming intensities, causing the power ratio for the two-beam non-symmetrical emitting for the corresponding Sample 3 to be not equal to unity. Nevertheless, we find that the power ratio for the two-beam non-symmetrical emitting for Sample 3 could be adjusted to unity, as along as the corresponding Samples 1 and 2 are with appropriate groove numbers. For instance, for the same Sample 3 in Fig. 7(a), we replace its groove

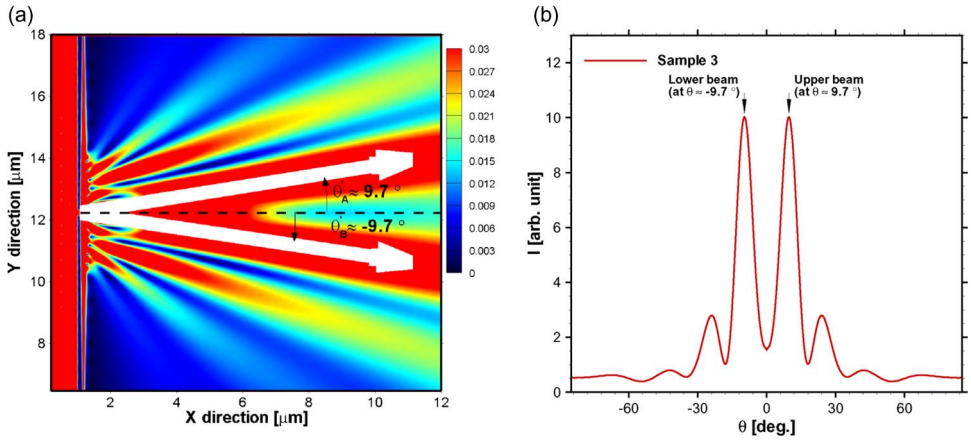


Fig. 8. (a) Magnetic field intensity $|H_z|$ distribution for the same Sample 3 in Fig. 6(g). The corresponding angular transmittance distribution $I$ is shown as the red curve in (b).

number with $[(n_{U_1}; n_{L_1}), (n_{U_2}; n_{L_2})] = [(4; 4), (10; 10)]$ to form another Sample 3 as is shown in Fig. 6(d), and the corresponding angular transmittance distribution is shown as the green curve in Fig. 7(a2). From this green curve, it is seen that the power ratio has been adjusted to be nearly unity, which is between $T \approx 8.9$ for the major peak at $\theta \approx 36.6^\circ$ and $T \approx 8.8$ for the one at $\theta \approx 14.4^\circ$.

In the same way, we replace the groove number for the same Samples 3 in Fig. 7(b) and (c) with $[(n_{U_1}; n_{L_1}), (n_{U_2}; n_{L_2})] = [(5; 5), (8; 8)]$ and [(5; 5), (13; 13)] as is shown in Fig. 6(e) and (f), respectively. The angular transmittance distributions for the former and the later cases are shown as the green curves in Fig. 7(b2) and (c2), respectively. Similarly, with appropriate groove numbers, these green curves show that the power ratios for both samples also could be tuned to almost unity. Note that in Fig. 7(b2), the ratio is between $T \approx 8.2$ for the major peak at $\theta \approx -7.8^\circ$ and $T \approx 8.2$ for the major peak at $\theta \approx 35.2^\circ$, and in Fig. 7(c2), the ratio is between $T \approx 8.5$ at $\theta \approx 35.7^\circ$ and $T \approx 8.4$ at $\theta \approx 3.1^\circ$.

The above results demonstrate that the power ratio for the two-beam non-symmetrical emitting for Sample 3 could be adjusted to be nearly unity by changing the groove numbers. This is due to the beaming intensities for Samples 1 and 2 can be adjusted via fine-tuning the numbers of their surrounding grooves. The corresponding magnetic field intensities for the above-mentioned Samples 3 with $[(n_{U_1}; n_{L_1}), (n_{U_2}; n_{L_2})] = [(4; 4), (10; 10)]$, [(5; 5), (8; 8)], and [(5; 5), (13; 13)] are shown in Fig. 7(a3), (b3), and (c3), respectively. From Fig. 7(a3), (b3), and (c3), it is seen that Samples 3 still produce clear two-beam non-symmetrical emitting like Types I, II, and III in Fig. 7(a1), (b1), and (c1), respectively, even if the surrounding groove numbers are changed.

Finally, we investigate the beaming phenomenon for Sample 3 that is formed by combining Samples 1 and 2 with $p_{U_1} = p_{L_2}$ and $p_{U_2} = p_{L_1}$. As an example, we select the parameters for Sets A and B from Table 1 as the groove periods for Samples 1 and 2 to form Sample 3 as is shown in Fig. 6(g), respectively. The magnetic field intensity distribution is shown in Fig. 8(a). Fig. 8(a) clearly shows that Sample 3 produces two-beam symmetrical emitting for the transmitted light emitted from the slit. From the two major peaks of the red curve for the angular transmittance distribution in Fig. 8(b), the splitting angles for the two-beam symmetrical emitting in Fig. 8(a) can be seen. As expected, the two splitting angles for the upper and the lower beams for Sample 3, i.e., $\theta'_A \approx 9.7^\circ$ and $\theta'_B \approx -9.7^\circ$, are very close to the beaming angles for the corresponding Samples 1 and 2, i.e., $\theta_A \approx 10.7^\circ$ and $\theta_B \approx -10.7^\circ$ as summarized in Table 1 for Sets A and B, respectively. Accordingly, one may conclude that Sample 3 with mixed-period grooves also could produce symmetrical multiple beams with desired splitting angles. Of course, the groove pitches of the surrounding mixed-period grooves should be symmetric and carefully designed.

## 4. Concluding Remarks

In conclusion, we have proposed a slit-groove-based structure called the MPSG structure for achieving two-beam non-symmetrical or symmetrical emitting for light emerged from a subwavelength structure. Our FDTD numerical results for the beaming phenomena are consistent with the theoretical results given by the surface plasmon diffraction theory. Then we have investigated the beaming phenomena for the MPSG structure, and the obtained results for the proposed structure can be summarized as follows. (1) By combining two typical slit-groove structures, two-beam non-symmetrical or symmetrical emitting can be created for the combined slit-groove MPSG structure. (2) The two-beam emitting phenomena for Sample 3 possess splitting angles which are close to the beaming angles of the unidirectional beaming phenomena for Samples 1 and 2. (3) The power ratio of the two-beam non-symmetrical emitting can be adjusted to almost unity by fine-tuning the number of the surrounding grooves of the MPSG structure to an appropriate value. In addition, our FDTD results for the two-beam emitting phenomena demonstrate that not only the periodic but also the non-periodic grooves could be used to produce significant directional beaming as long as the non-periodic groove pitches are carefully designed. Owing to the flexibility for producing two-beam non-symmetrical and symmetrical emitting, we believe the presented MPSG structure will have potential applications in compact beam-splitters for use in miniatured photonic integrated circuits.

## References


[1] E. Ozbay, "Plasmonics: Merging photonics and electronics at nanoscale dimensions," *Science*, vol. 311, no. 5758, pp. 189–193, Jan. 2006.

[2] H. J. Lezec, A. Degiron, E. Devaux, R. A. Linke, L. Martin-Moreno, F. J. Garcia-Vidal, and T. W. Ebbesen, "Beaming light from a subwavelength aperture," *Science*, vol. 297, no. 5582, pp. 820–822, Aug. 2002.

[3] H. Caglayan, I. Bulu, and E. Ozbay, "Plasmonic structures with extraordinary transmission and highly directional beaming properties," *Microw. Opt. Technol. Lett.*, vol. 48, no. 12, pp. 2491–2496, Dec. 2006.

[4] A. I. Fernández-Domínguez, E. Moreno, L. Martín-Moreno, and F. J. García-Vidal, "Beaming matter waves from a subwavelength aperture," *Phys. Rev. A*, vol. 74, no. 2, pp. 021601-1–021601-4, Aug. 2006.

[5] J. Christensen, L. Martín-Moreno, and F. J. García-Vidal, "Enhanced acoustical transmission and beaming effect through a single aperture," *Phys. Rev. B*, vol. 81, no. 17, pp. 174104-1–174104-6, May 2010.

[6] L. Martín-Moreno, F. J. García-Vidal, H. J. Lezec, A. Degiron, and T. W. Ebbesen, "Theory of highly directional emission from a single subwavelength aperture surrounded by surface corrugations," *Phys. Rev. Lett.*, vol. 90, no. 16, pp. 167401-1–167401-4, Apr. 2003.

[7] C. Wang, C. Du, Y. Lv, and X. Luo, "Surface electromagnetic wave excitation and diffraction by subwavelength slit with periodically patterned metallic grooves," *Opt. Exp.*, vol. 14, no. 12, pp. 5671–5681, Jun. 2006.

[8] Y. Liu, H. Shi, C. Wang, C. Du, and X. Luo, "Multiple directional beaming effect of metallic subwavelength slit surrounded by periodically corrugated grooves," *Opt. Exp.*, vol. 16, no. 7, pp. 4487–4493, Mar. 2008.

[9] B. Lee, S. Kim, H. Kim, and Y. Lim, "The use of plasmonics in light beaming and focusing," *Prog. Quant. Electron.*, vol. 34, no. 2, pp. 47–87, Mar. 2010.

[10] D. Z. Lin, C. K. Chang, Y. C. Chen, D. L. Yang, M. W. Lin, J. T. Yeh, J. M. Liu, C. H. Kuan, C. S. Yeh, and C. K. Lee, "Beaming light from a subwavelength metal slit surrounded by dielectric surface gratings," *Opt. Exp.*, vol. 14, no. 8, pp. 3503–3511, Apr. 2006.

[11] D. Z. Lin, T. D. Cheng, C. K. Chang, J. T. Yeh, J. M. Liu, C. S. Yeh, and C. K. Lee, "Directional light beaming control by a subwavelength asymmetric surface structure," *Opt. Exp.*, vol. 15, no. 5, pp. 2585–2591, Mar. 2007.

[12] S. Kim, H. Kim, Y. Lim, and B. Lee, "Off-axis directional beaming of optical field diffracted by a single subwavelength metal slit with asymmetric dielectric surface gratings," *Appl. Phys. Lett.*, vol. 90, no. 5, pp. 051113-1–051113-3, Jan. 2007.

[13] H. Caglayan, I. Bulu, and E. Ozbay, "Observation of off-axis directional beaming via subwavelength asymmetric metallic gratings," *J. Phys. D. Appl. Phys.*, vol. 42, no. 4, pp. 045105-1–045105-4, Feb. 2009.

[14] Y. Yuan, J. Liu, J. He, and J. Yao, "Directional terahertz beams realized by depth-modulated metallic surface grating structures," *J. Opt. Soc. Amer. B*, vol. 28, no. 11, pp. 2674–2679, Nov. 2011.

[15] F. Hao, R. Wang, and J. Wang, "A design methodology for directional beaming control by metal slit–grooves structure," *J. Opt.*, vol. 13, no. 1, pp. 015002-1–015002-4, Jan. 2011.

[16] F. Hao, M. Zhang, Q. Wang, J. Wang, R. Wang, and H. Ge, "Design and experimental demonstration of a plasmonic directional beaming device," *J. Opt. Soc. Am. B*, vol. 29, no. 8, pp. 2255–2259, Aug. 2012.

[17] F. J. Garcia-Vidal, H. J. Lezec, T. W. Ebbesen, and L. Martin-Moreno, "Multiple paths to enhance optical transmission through a single subwavelength slit," *Phys. Rev. Lett.*, vol. 90, no. 21, pp. 213901-1–213901-4, May 2003.

[18] F. J. Vidal, H. J. Lezec, and T. W. Ebbesen, "Focusing light with a single subwavelength aperture flanked by surface corrugations," *Appl. Phys. Lett.*, vol. 83, no. 22, pp. 4500–4502, Dec. 2003.

[19] C. Wang, C. Du, and X. Luo, "Refining the model of light diffraction from a subwavelength slit surrounded by grooves on a metallic film," *Phys. Rev. B*, vol. 74, no. 24, pp. 245403-1–245403-7, Dec. 2006.

[20] L. B. Yu, D. Z. Lin, Y. C. Chen, Y. C. Chang, K. T. Huang, J. W. Liaw, J. T. Yeh, J. M. Liu, C. S. Yeh, and C. K. Lee, "Physical origin of directional beaming emitted from a subwavelength slit," *Phys. Rev. B*, vol. 71, no. 4, pp. 041405-1–041405-4, Jan. 2005.
[21] S. Kim, Y. Lim, J. Park, and B. Lee, "Bundle beaming from multiple subwavelength slits surrounded by dielectric surface gratings," *J. Lightwave Technol.*, vol. 28, no. 14, pp. 2023–2029, Jul. 2010.
[22] H. B. Chen, X. S. Chen, J. Wang, and W. Lu, "Tunable beam direction and transmission of light using photonic crystal waveguide," *Phys. B*, vol. 403, no. 23/24, pp. 4301–4304, Dec. 2008.
[23] Y. Zhang, D. Zhao, C. Zhou, and X. Jiang, "Directional light emission through a metallic nanostructure," *J. Appl. Phys.*, vol. 105, no. 11, pp. 113124-1–113124-6, Jun. 2009.
[24] Q. Wang, L. Zhang, and Q. Li, "Beam splitting at the output of photonic crystal waveguides with discrete surface point defects," *Opt. Exp.*, vol. 18, no. 23, pp. 24245–24257, Nov. 2010.
[25] W. Jia, L. Jiang, K. Chen, and X. Li, "Design of photonic crystal power beam splitters via corrugated and gratinglike surfaces," *Opt. Commun.*, vol. 283, no. 20, pp. 4078–4084, Oct. 2010.
[26] W. Jia, J. Deng, H. Wu, X. Li, and A. J. Danner, "Design and fabrication of high-efficiency photonic crystal power beam splitters," *Opt. Lett.*, vol. 36, no. 20, pp. 4077–4079, Oct. 2011.
[27] C. Zhou and P. Kohli, "Ultracompact beam splitters based on plasmonic nanoslits," *J. Appl. Phys.*, vol. 109, no. 9, pp. 093114-1–093114-6, May 2011.
[28] Y. Wang, D. H. Zhang, J. Wang, M. Yang, D. Li, and Z. Xu, "Beam splitting with subwavelength resolution using combined metallodielectric films," *J. Opt. A, Pure Appl. Op.*, vol. 14, no. 1, pp. 015103-1–015103-4, Jan. 2012.
[29] H. Raether, *Surface Plasmons on Smooth and Rough Surfaces and on Gratings,* 1st ed. Berlin, Germany: Springer-Verlag, 1988, p. 5.
[30] A. Taflove and S. C. Hagness, *Computational Electrodynamics: The Finite-Difference Time-Domain Method,* 3rd ed. Norwood, MA, USA: Artech House, 2005.
[31] D. W. Lynch and W. R. Hunter, "SILVER (Ag)," in *Handbook of Optical Constants of Solids*, E. D. Palik, Ed. New York, NY, USA: Academic, 1985, pp. 350–357.
[32] H. W. Kihm, K. G. Lee, D. S. Kim, J. H. Kang, and Q. H. Park, "Control of surface plasmon generation efficiency by slit-width tuning," *Appl. Phys. Lett.*, vol. 92, no. 5, pp. 051115-1–051115-3, Feb. 2008.
[33] P. Lalanne, J. P. Hugonin, and J. C. Rodier, "Theory of surface plasmon generation at nanoslit apertures," *Phys. Rev. Lett.*, vol. 95, no. 26, pp. 263902-1–263902-4, Dec. 2005.